



Geometric-confinement suppression of flow-boiling instability using perforated wick: Part I CHF and conductance enhancement

Júlio Ferreira, Massoud Kaviany*

Department of Mechanical Engineering, University of Michigan, Ann Arbor, MI, 48109, United States

ARTICLE INFO

Article history:

Received 27 March 2020

Revised 12 May 2020

Accepted 13 May 2020

Available online 29 June 2020

Keywords:

Flow boiling

Extreme heat flux

Perforated canopy wick with levees

Hydrodynamic instability

Geometric confinement

Critical heat flux

Heat transfer coefficient

ABSTRACT

Bubbles formed in flow boiling merge and pickup momentum downstream and inhibit liquid supply to the heated surface. To investigate these competitions between the phases adjacent to the heated surface (hydrodynamic instabilities) and to establish leading-edge liquid supply tracks, the flow-boiling canopy wick (FBCW) was previously introduced. The FBCW is a periodic, 3-D porous (sintered, metallic powder) and perforated structure enabling capillary suction to optimally separate and direct the liquid and vapor paths adjacent to the heated surface, while the liquid track is formed between the periodic perforations.

Here, addition of levees (geometric confinement) on the edge of the perforations ensures the hydrodynamic stability (by diverting the vapor stream and wall-stabilizing the liquid track), thus extending the liquid track between the levees. The irrigated canopy is connected to porous posts and monolayer-evaporator for liquid supply and the vapor generated over the monolayer wick escapes through the perforations. This thin evaporation wick results in large thermal conductance. The critical heat flux (CHF) or dryout limits (e.g., liquid-vapor hydrodynamic instability, capillary-viscous) of this leveed FBCW are examined using analytical and numerical (CFD, including the VOF technique) simulations. The CFD results for saturated water at 1 atm and for a horizontal, rectangular channel heated at the lower surface show the surface liquid track is stabilized by the levees and the flow-boiling CHF and thermal conductance are enhanced significantly beyond the plain surface, reaching the capillary-viscous dryout limit. The leading-edge liquid track irrigation of the wick allows for use of smaller liquid velocities. The results for the FC-72 fluid are also presented.

© 2020 Elsevier Ltd. All rights reserved.

1. Introduction

Boiling heat transfer allows for high heat flux at small thermal resistance (large thermal conductance). Due to the random nature of vapor bubbles generated, a threshold is reached where the supply of the liquid to the heated surface is interrupted, leading to hydrodynamic-controlled dryout, i.e., the critical heat flux (CHF), which is followed by a rapid increase in the surface temperature. The flow-boiling canopy wick (FBCW) applied to the lower surface of a horizontal saturated liquid stream channel, shown in Fig. 1(a), was introduced [1] to replace this chaotic bubble formation with meniscus-surface evaporation in a thin wick, creating separated and directed paths for the liquid and vapor phases. The FBCW unit cell is shown in Fig. 1(b) with all relevant geometric parameters. The symbols are defined in the nomenclature. The main compo-

ments of this 3-D wick are the porous perforated canopy, posts and monolayer. These hold the liquid while allowing the vapor generation on top of the monolayer to escape through the perforations into the channel where the liquid flows.

In the FBCW, the canopy separates the liquid stream from the vapor space, however, the vapor escaping through the perforations mixes with the liquid above the canopy. This creates a two-phase hydrodynamic-stability controlled CHF above the canopy. The primary instability is related to the leading-edge liquid track which supplies the liquid to canopy which directs it to the evaporator (monolayer) through the posts. At high heat flux, the accumulated vapor flowing above this liquid track causes a shear instability. Below the canopy, the capillary-viscous controlled CHF governs the liquid permeation, evaporation and vapor venting.

The FBCW structure is periodic in two directions, and its simplest unit cell will contain four permeable posts, a perforated, permeable canopy, and a thin, single-layer sintered-particle (monolayer) wick covering the heated surface [Fig. 1(a)]. The monolayer has an optimal permeability and capillary pressure and spreads the

* Corresponding author.

E-mail address: kaviany@umich.edu (M. Kaviany).

Nomenclature

A	area (m ²)
C	inertial coefficient
c_d	discharge coefficient
c_p	heat capacity (J/kg-K)
D, d	diameter (m)
f	friction factor
Fr	Froude number
G/A	thermal conductance [K/(W/m ²)]
g	gravitational acceleration (m/s ²)
H, h	height (m)
Δh_{lg}	heat of evaporation (kJ/kg)
K	permeability (m ²)
k	thermal conductivity (W/m-K)
k_B	Boltzmann constant (J/K)
L, l	length, thickness (m)
\dot{M}	mass flow rate (kg/s)
M	molecular weight (kg/mol)
\dot{m}	mass flux (kg/m ² -s)
Ma	Mach number
$N_{p,x}$	number of posts
p	pressure (Pa)
P	perimeter (m)
Q	heat flow rate (W)
q	heat flux (W/m ²)
Re	Reynolds number
t	time (s)
T	temperature (K)
\mathbf{u}	velocity vector (m/s)
u	axial velocity (m/s)
u_a	speed of sound (m/s)
v	vertical velocity (m/s)
W, w	width (m)
We	Weber number
x	spatial coordinate (m), quality
y	spatial coordinate (m)
z	spatial coordinate (m)
Z	dimensionless figure of merit

Greek symbols

α	void fraction
γ	heat capacity ratio, aspect ratio
Δ	difference, drop
Δ_p	lateral post spacing (m)
δ	thickness (m)
ϵ	porosity
κ	wavenumber (1/m)
λ	wavelength (m)
μ	viscosity (Pa-s)
ρ	density (kg/m ³)
σ	surface tension (N/m)
τ	shear stress (N/m ²)
ϕ	generic variable
θ_c	contact angle (°)

Subscripts

ch	choked flow
CHF	critical heat flux
Cu	copper
c	capillary, cell
ca	canopy
ch	channel
$c - v$	capillary-viscous

f	flooding
$FBCW$	flow-boiling canopy wick
g	gas
h	heater
l	liquid
lg	liquid-gas phase change
m	monolayer
max	maximum
n	nucleation
o	baseline
p	post
ps	plain surface
per	perforation
sh	superheat
s	surface
Z	Zuber
Others	
$\langle \rangle$	spatial average
$-$	temporal average
$*$	dimensionless

liquid supplied through the posts. The aim is to create and maintain a vapor space for steady and uniform film evaporation over the heated surface, while allowing for uninterrupted liquid supply represented by the leading-edge liquid track and the vapor escape.

The CHF is the most important limit in flow-boiling, representing the upper limit for a safe operation [2]. The treatments of the flow-boiling CHF, however, have been mostly empirical, due to the complexity of the two-phase flow, and until recently there has not been a theoretical treatment comparable to that of the Zuber for the pool-boiling CHF [3]. Even the empirical correlations have been limited to a specific range of parameters not suited for different experimental conditions. The underlying thermal-hydraulic mechanisms triggering the flow-boiling CHF have been addressed in [3] and more recently in [4].

Two suggested mechanisms (models) for horizontal, heated surfaces are rendered in Fig. 2. In the *liquid-vapor, boundary-layer interfacial separation dryout* [5,6] model the flow boiling crisis is treated as a purely hydrodynamical phenomenon, analogous to the single-phase flow with gas injection at the heated surface. The generated vapor decreases the liquid velocity gradient adjacent to the surface, making this gradient to gradually diminish causing the separation of the liquid layer and dryout.

In the *vapor-liquid separated flow interfacial lift-off dryout* [7,8] model the liquid supply to the surface is limited to the small wetting fronts in between long vapor patches covering the surface. The dryout occurs when the momentum of the vapor generated in the wetting front overcomes the interfacial pressure force, lifting the liquid away from the heated surface. A recent extended version of this model accounts for instabilities perpendicular to the surface similar to the Zuber treatment for pool boiling [9]. The calculation of the CHF requires the implementation of a separated flow model described in Part II Section 1 [13].

These have treated the plain surface, where bubbles are formed randomly and intermittently (as compared to the perforated canopy wick that creates continuous vapor stream from through the perforations), so the leading-edge liquid track cannot be characterized.

Here we introduce levees around the perforations to protect the leading-edge liquid track (and increase the dryout limit) from the axial vapor acceleration which combined with the liquid perme-

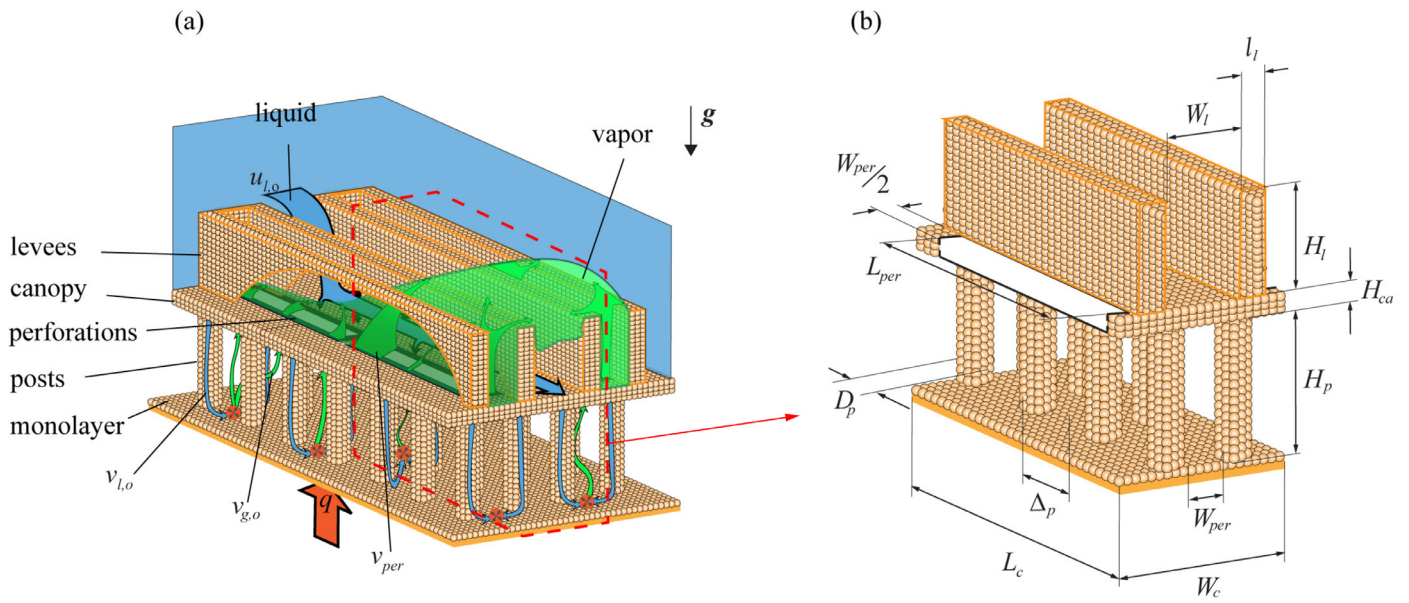


Fig. 1. (a) Schematic of the FBCW with levees showing the monolayer, posts, the perforated canopy, and the vapor path through the perforations into the liquid stream. The levees on top of the canopy divert this escaping vapor stream and confine the leading-edge liquid track. (b) The FBCW unit cell showing the geometric parameters of the channel and the wick. The symbols are defined in the nomenclature.

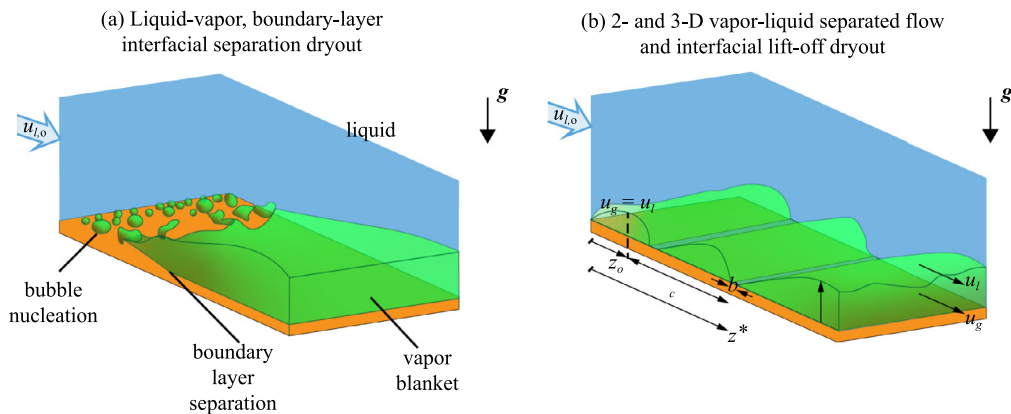


Fig. 2. Two of the suggested CHF trigger mechanisms for flow boiling over a heated, plain surface horizontal surface. (a) Boundary-layer separation [5,6]. (b) Interfacial lift-off [7,8].

ation toward the evaporator lead to thinning of the liquid track and its instability [10,11]. By eliminating the competition between the phases close to the heated surface and allowing for a continuous supply of the liquid through its capillary structure, the FBCW aims to control and enhance the CHF and the thermal conductance

2. Dryout limits for the FBCW with levees

The related CHF (surface dryout) mechanisms in the FBCW are shown schematically in Fig. 3.

Capillary-viscous limit, $q_{CHF,c-v}$: the maximum capillary pressure (occurs in the monolayer) balanced by the summation of all viscous and inertial pressure drops occurring along the liquid and vapor paths (which depend on the mass flux).

Liquid-vapor hydrodynamic limit, $q_{CHF,lg}$: liquid-vapor interactions (and instabilities) above the canopy wick hindering the liquid supply to evaporator.

Liquid superheat limit, $q_{CHF,sh}$: the liquid inside the monolayer wick is superheated (ΔT_{sh}) and when this superheat exceeds a

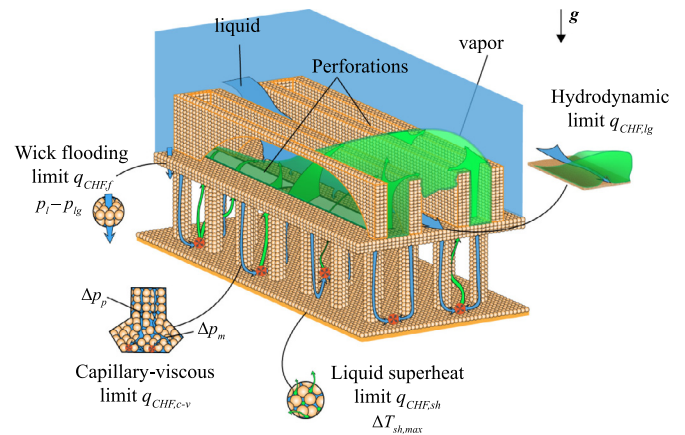


Fig. 3. Schematic representation of the four most relevant flow-boiling CHF limits when using the FBCW with levees. Hydrodynamic limit, above the canopy. Capillary-viscous and liquid superheat limits, below the canopy.

maximum $\Delta T_{sh,max}$, then bubbles are formed in the wick and hinder the liquid flow and cause dryout.

Wick flooding limit, $q_{CHF,f}$: when the dynamic pressure difference across the canopy wick is large enough to force extra (over the capillary-driven flow) liquid toward the heated surface. It is not a main concern for the FBCW.

Vapor kinetic theory limit, q_{max} : the theoretical upper limit of the vapor mass flux (one-dimensional molecular or thermal flow) due to evaporation.

Vapor choking limit, $q_{CHF,ch}$: the vapor from the monolayer wick surface flows through the vapor space and to the perforations, and this reduction in flow cross-section area increases the velocity from $v_{g,m}$ to $v_{g,per}$ and can reach the sonic limit.

Vapor compressibility limit, $q_{CHF,Ma}$: our analysis assumes incompressible flows, so the vapor Mach number $Ma_{g,per}$ is kept below 0.3. So, we use the vapor compressibility limit which is more restrictive compared to the vapor choking limit.

The capillary-viscous limit and the hydrodynamic limit are the most relevant and will be discussed below. The other limits were first discussed in previous works [1,12] and are detailed in Part II Section 2 [13].

3. Wick side CHF and thermal conductance

The CHF limits below the canopy (capillary-viscous, liquid superheat) are controlled by the wick. For a given heat flux q , constant liquid supply on the canopy surface is assumed along with the evaporation rate on the monolayer wick. Both 3-D CFD and 1-D network transport models are used for the prediction of the liquid and vapor flows. The wick properties (volume average such as the permeability, capillary pressure, and effective thermal conductivity) are found from bulk relationships or from direct (pointwise) numerical simulation. The details are given in Part II Section 3 [13]. The capillary pressure and wick permeability are related to the capillary-viscous limit, discussed in Subsection 3.1, and the effective thermal conductivity is related to both the superheat limit and the wick thermal conductance, discussed in Subsection 3.2. Subsection 3.3 introduces the CFD modelling utilized in this study.

3.1. Capillary-viscous limit

The FBCW is made of monosized spherical copper particles of diameter d_m and sintered to a porosity of ϵ_m in the monolayer, ϵ_p in the posts, and ϵ_{ca} in the canopy. The capillary-viscous limit depends on the maximum capillary pressure which occurs in the monolayer, and the summation of liquid and vapor pressure drops in the 3-D canopy wick. The canopy wick is the ensemble of three wicks:

Perforated canopy wick: perforated porous layer which separates the inertia-dominated two-phase flow above it from the capillary-dominated, separated liquid and gas flows. The periodic perforation slots allow for the vapor venting and formation of the leading-edge liquid track.

Post wicks: porous columns arranged as anisotropic unit cell and between the perforations, with their lateral spacing limited by the perforation width. The parameters are the post diameter D_p , post spacing Δ_p , the number of posts along the perforation $N_{p,x}$, and the perforation width W_{per} . The perforation width is limited by the capillary length [14]

$$l_c = \left(\frac{\sigma \cos \theta_c}{\Delta \rho_l g} \right)^{1/2}, \quad (1)$$

and for water, this is 2.1 mm, at saturation temperature ($p = \text{atm}$). Here we use $W_{per} = 1.5$ mm to ensure no liquid penetration through the perforations during a startup condition. The unit

Table 1

The FBCW geometric parameters shown in Fig. 1 written in terms of the post diameter D_p , post spacing Δ_p , the number of posts along the perforation $N_{p,x}$, and the perforation width W_{per} .

$W_c = 2(W_{per} + D_p)$	$A_{base} = W_c L_c$
$L_c = L_{per} + D_p$	$A_{per} = W_{per} L_{per}$
$l_w = (L_p - D_p)/3$	$A_{ca} = A_{base} - A_{per}$
$W_l = 2D_p + W_{per}$	$A_{po} = N_{p,x} \pi D_p^2 / 4$
$l_{per} = D_p$	

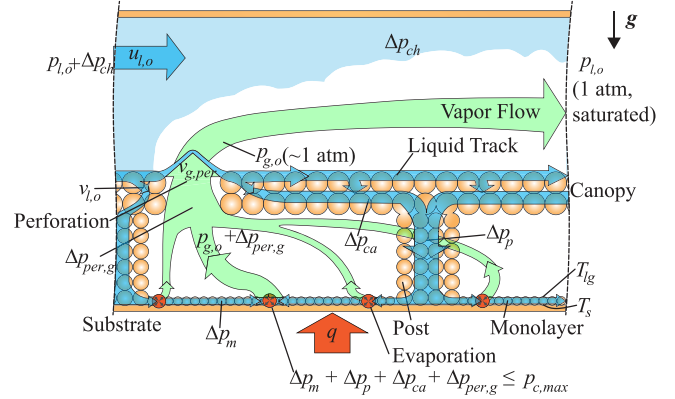


Fig. 4. Schematic representation of viscous and inertial pressure drop components along the liquid and vapor paths in the wick side.

cell has two posts along the perforation and an additional post between each perforation ($N_{p,x}=3$), the axial perforation length is

$$L_{per} = N_{p,x} \Delta_p + (N_{p,x} - 1) D_p. \quad (2)$$

Monolayer wick: ideally a single layer of close-packed, sintered spherical diameter particles covering the heated surface and allowing for evaporation. It has an effective conductivity that along with the wick small thickness results in large thermal conductance (details are discussed in Part II). The monolayer unit cell is centered around the post and it has an equivalent diameter

$$L'_p = \left[\frac{4}{\pi} (W_{per} + D_p) (\Delta_p + D_p) \right]^{1/2}. \quad (3)$$

Table 1 summarizes the FBCW geometric parameters. The optimal parameters $N_{p,x}$ and Δ_p alongside with the overall optimization of the wick geometry are discussed further in Part II Section 4 [13]

The capillary-viscous CHF $q_{CHF,c-v}$ is the upper limit for the FBCW performance imposed by the wick. It is the threshold when the summation of all wick component viscous pressure drops (canopy, posts, and monolayer) and the vapor inertial pressure drop balance the maximum capillary pressure in the monolayer, i.e.,

$$\Delta p_m + \Delta p_p + \Delta p_{ca} + \Delta p_{per,g} = p_{c,max}, \quad (4)$$

these liquid and vapor paths and the respective pressure drops are depicted in Fig. 4. The maximum capillary pressure is obtained from the relation in [15].

The viscous pressure drop components are given by the Darcy law [14] (with volume-averaged properties calculations discussed in Part II)

$$\Delta p = \frac{\mu \langle u \rangle}{\langle K \rangle} L. \quad (5)$$

Phase velocities in the different wick components are calculated from the imposed heat flux and geometric relationships as

$$v_{l,o} = \frac{q}{\rho_l \Delta h_{lg}} \frac{A_{base}}{A_{ca}}, \quad v_{l,po} = \frac{q}{\rho_l \Delta h_{lg}} \frac{A_{base}}{A_{po}}, \quad v_{g,o} = \frac{q}{\rho_g \Delta h_{lg}} \frac{A_{base}}{A_{per}}. \quad (6)$$

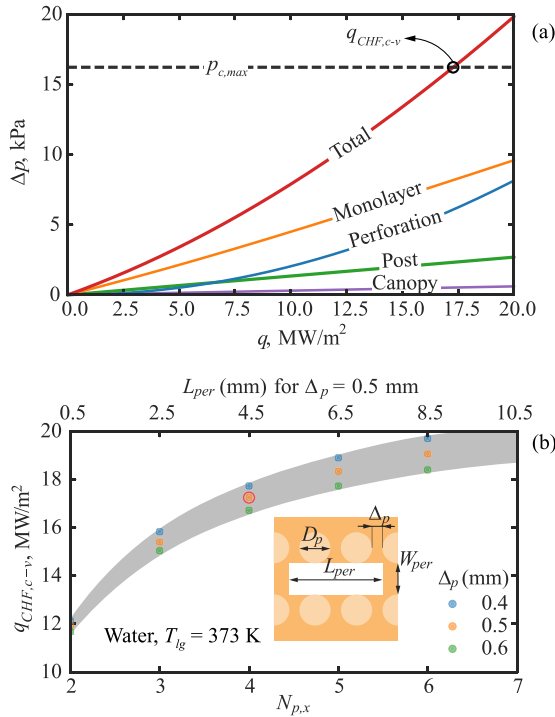


Fig. 5. (a) Variations of the various pressure drops with heat flux. The monolayer and vapor perforation pressure drops dominant. The optimized wick capillary-viscous CHF is also shown. (b) Variation of $q_{CHF,c-v}$ with $N_{p,x}$ for different Δ_p (for water).

A finite-volume network model is used for the monolayer properties varying with the meniscus thickness.

The inertial pressure for vapor passing through a perforation is [16]

$$\Delta p_{per,g} = \frac{1}{2} C \rho_g v_{g,o}^2, \quad (7)$$

where the inertial coefficient is

$$C = \left[\frac{1.642}{A^* (1 - A^{*2.6}) (1 + l^{*3.5} + A^{*3.6})} - 1 \right]^2, \quad (8)$$

and $A^* = A_{per}/A_{base}$ and $l^* = l_{per}/D_{per}$.

Rewriting Eq. (4), the capillary-viscous CHF can be written as a function of the pressure drop components

$$A^{*2} \frac{C}{2\rho_g \Delta h_{lg}^2} q_{CHF,c-v}^2 + \frac{\mu_l}{\rho_l \Delta h_{lg}} \left[\frac{(L'_p - D_p)/3}{K_m} \frac{4L'_p{}^2}{\langle \delta \rangle_m (L'_p + D_p)/2} \right] \times q_{CHF,c-v} = p_{c,max}, \quad (9)$$

further details on this derivation are given in Part II Section 3 [13].

Figure 5 (a) presents the variation of pressure drops with imposed heat flux. As expected, higher capillary pressure is needed for higher q . Based on the optimized wick parameters shown in Fig. 5(b), the capillary-viscous limit is $q_{CHF,c-v} = 17 \text{ MW/m}^2$ for a $p_{c,max} = 16.2 \text{ kPa}$.

3.2. FBCW Thermal conductance

The thermal conductance of the FBCW depends on the monolayer effective conductivity $\langle k \rangle_m$ and the meniscus height $\langle \delta \rangle_m$, shown in Fig. 6(a), i.e.,

$$\langle q \rangle = -\langle k \rangle_m \frac{A_m}{A} \frac{T_s - T_{lg}}{\langle \delta \rangle_m} = \frac{G}{A} (T_s - T_{lg}). \quad (10)$$

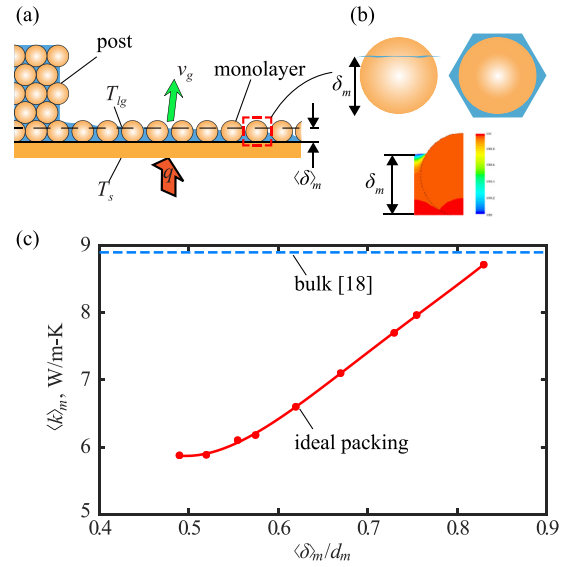


Fig. 6. (a) Schematic representation of the evaporation on the monolayer showing the variation of the meniscus thickness. (b) Unit-cell meniscus for hexagonal packing obtained using the Surface Evolver code. Snapshots of temperature distribution in the particle and liquid, the copper-water interface is shown with broken line. (c) Variation of the effective thermal conductivity with the average meniscus thickness.

The heat conducts through the monolayer wick with its pores occupied by liquid. The meniscus adjusts its topology according to the capillary pressure and Fig. 6(b) shows the equilibrium surface for a given pressure, obtained with the meniscus surface computation code Surface Evolver [17]. The variation of the computed effective conductivity is shown in Fig. 6(c) as a function of the average meniscus thickness, for water and copper particle (closely packed). The Hadley [18] correlation is used for the bulk effective thermal conductivity. The simulations use the Star-CCM+ [19] code using symmetry (1/12th geometry) with mesh size of $0.02d_m$. The boundary conditions are prescribed temperature T_s at the base of the particle and the liquid, prescribed temperature T_{lg} on the meniscus, and adiabatic elsewhere. The solid-liquid interfacial coupling uses the conjugate heat transfer. The bulk effective thermal conductivity from the correlation in [14] is also shown. The effective thermal conductivity is higher at lower capillary pressures (larger average meniscus thickness), and the heat flows mainly within the particle. The monolayer effective thermal conductivity is about ten folds larger than that of liquid water, greatly increasing the thermal conductance to $150 \text{ kW/m}^2\text{-K}$.

3.3. CFD Simulation of wick liquid flow

The 2x6 perforations canopy wick simulated (CFD) for both the wick liquid flow and the channel two-phase flow hydrodynamics using Ansys Fluent [20] is shown in Fig. 7. The CFD simulation details are given in Part II Section 5 [13], which include the volume-averaged properties. The boundary conditions for the 3-D wick flow simulations and a typical flow traced by the streamlines are shown in Fig. 7. The pressure drop from the 1-D network model have been compared with these 3-D results and good agreement has been found. Since the monolayer permeability varies with the local meniscus thickness (which depends on heat flux), more accurate results are expected from the point-wise numerical treatment where the variation of the meniscus thickness is tracked and a variable local permeability is used. However overall, the 1-D network and the 3-D CFD results suffice to predict the wick liquid flow relatively accurately. These CFD results of the liquid flow in the canopy wick are combined with the CFD results in

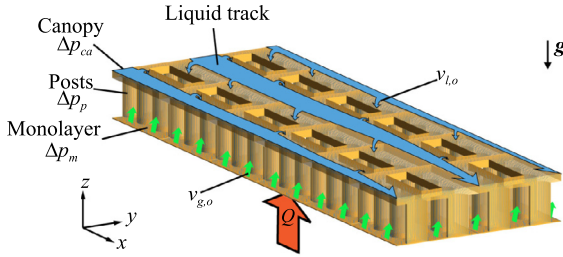


Fig. 7. The 2x6 perforations canopy wick simulated (CFD) for the wick liquid flow, showing the boundary conditions (irrigation from the channel flow and evaporation on the monolayer). Typical streamlines for the liquid flow through the perforated canopy, posts, and monolayer are also shown.

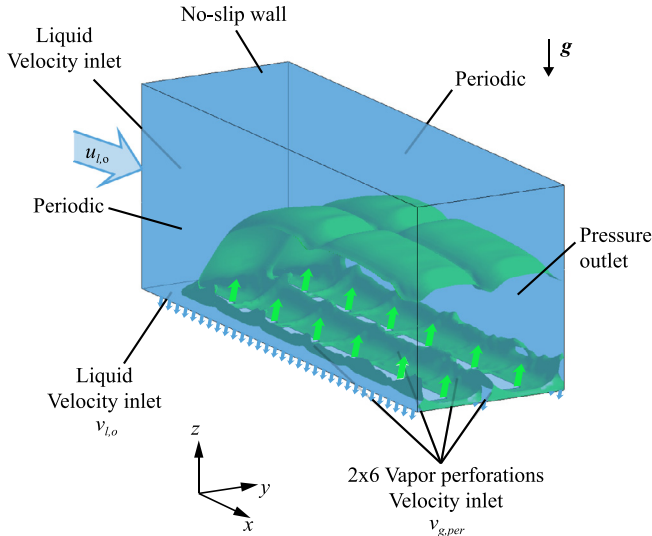


Fig. 8. The 2x6 perforations canopy wick simulated (CFD) for the channel two-phase flow, showing the boundary conditions (irrigation of the wick and vapor escaping from the perforations).

Section 4, to render the combined behavior in videos presented in Section 6.

4. Channel-side CHF without levees

While aspects of the two-phase hydrodynamics above and the capillary-viscous thermal hydraulics below the canopy are intertwined, they can be separated to introduce independent control of the CHF. The very high CHF reported in [1] ($q = 20 \text{ MW/m}^2$ for liquid inlet velocity $u_{l,o} = 2 \text{ m/s}$) is valid for a rather short heater ($L_{ch} = 12 \text{ mm}$, i.e., only two axial perforations) and a single lateral perforation (with periodicity) used there. The addition of lateral vapor perforations introduces instabilities that greatly affect (lateral interfacial shearing) the leading-edge liquid track. Similarly, for longer heaters (additional axial perforations) it affects the liquid track dryout (axial interfacial shearing) by progressive downstream increase of the vapor mass flow rate). In this study, to minimize the lateral size effect, two lateral perforations with lateral periodic boundary conditions are used in the CFD simulations, shown in Fig. 8 (additional details of the CFD modelling are given in Part II Section 5). Also to include large enough heater length, we use six axial perforations with the continuity exit condition.

The hydrodynamics of the two-phase flow above the canopy involves the vapor escape from the perforations and merging with the liquid stream. The geometric parameters of the FBCW are shown in Fig. 1(b). The liquid inlet velocity and the vapor veloc-

ity exiting the perforation, and the direction of gravity are also shown there. The liquid and vapor inertial forces are scaled with their respective viscosities in the Reynolds number for the liquid and vapor phases. The role of the interfacial liquid-vapor surface tension is presented in the Weber number using the liquid inertia for scaling.

The role of gravity (buoyancy) is presented by the Froude number, again using the liquid inertia for scale. Since compressibility of the flowing vapor will be addressed, the Mach number using the vapor speed of sound for scale (for Mach number smaller than 0.3, the compressibility effect can be neglected). So, the hydrodynamic dimensionless numbers are the Reynolds numbers, the Weber, the Froude and Mach number, i.e., [21,22]

$$\text{Re}_l = \frac{\rho_l u_{l,o} W_{ch}}{\mu_l}, \quad \text{Re}_g = \frac{\rho_g v_{g,per} D_{per}}{\mu_g}, \quad \text{We}_D = \frac{\rho_l u_{l,o} D_h}{\sigma}, \quad (11)$$

$$\text{Fr}_{D,per} = \left[\frac{\rho_l u_{l,o}^2}{g(\rho_l - \rho_g) D_{per}} \right]^{1/2}, \quad \text{Ma}_{g,per} = \frac{v_{g,per}}{u_a},$$

here subscript l stands for liquid, g for vapor (gas), D_{per} is the perforation hydraulic diameter and u_a is the vapor speed of sound.

So, in general the hydrodynamic crises, including the dryout, are governed by these dimensionless parameters. In addition, for example when the Froude number is larger than unity, the role of gravity is less significant (compared to liquid inertia) and the liquid stream is able to carry the vapor axially.

4.1. Leading-edge liquid track and dryout

The leading-edge liquid track is that portion of the bulk of liquid stream that flows in contact with the perforated canopy, in between neighboring vapor-exit perforations. The liquid and vapor coexist and compete in the channel, and the vapor mass flow rate progressively increases downstream. This leads to a two-phase hydrodynamic-stability controlled CHF, i.e., the eventual breakup of this leading-edge liquid track, which then results in downstream track dryout (interruption of the supply of liquid to the evaporator through the wick). This breakup of the liquid track is observed in the CFD simulations and is due to vapor-liquid interfacial shear (Kelvin-Helmholtz).

Figure 9 shows the time evolution of the average leading-edge liquid track width with time at the outlet, for three different heat fluxes of 1.5, 2.0 and 2.5 MW/m^2 up to 1.5 times the liquid particle transit time (traveling the channel length), since no significant changes were observed after that. The results are for $u_{l,o} = 0.5 \text{ m/s}$. The liquid and vapor distributions at the exit of the channel (39 mm) are also shown on top with the corresponding snapshots. For $q = 2.5 \text{ MW/m}^2$, the liquid track width approaches zero, indicating discontinuity in the liquid supply to the wick. For lower heat fluxes, $q = 1.5 \text{ MW/m}^2$ and 2.0 MW/m^2 , there is continuous, non-zero liquid track width. Based on this, the predicted hydrodynamic limit for the FBCW without levees is around $q_{CHF,lg} = 2.0$ to 2.5 MW/m^2 . This is in general agreement with reported experimental results (for saturated water in vertical channel) of about 2 MW/m^2 for $u_{l,o} = 0.5 \text{ m/s}$ [23–25]. At large liquid velocities, i.e., large Froude number, the effect of gravity is reduced. For example for $u_{l,o} = 0.5 \text{ m/s}$, $\text{Fr}_{D,per} = 3.4$.

Further comparison of the CFD and experimental results will be presented in Section 6.

4.2. Kelvin-Helmholtz shear instability of leading-edge liquid track

We pursue that the FBCW hydrodynamic limit is caused by the vapor-liquid relative velocity, so the Kelvin-Helmholtz instability disrupts the liquid track [e.g., [11]]. This is illustrated by Fig. 10. The Kelvin-Helmholtz instability occurs under a threshold velocity

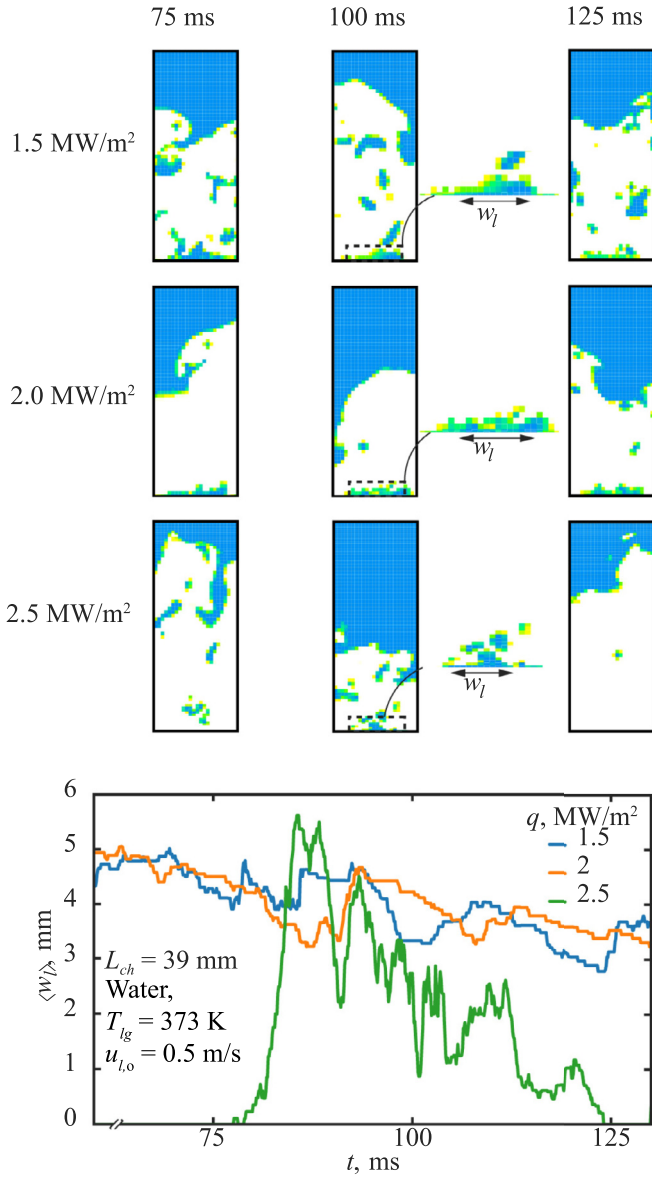


Fig. 9. Time variations of the average liquid track width at the channel outlet for three different heat fluxes. The corresponding snapshots of the outlet phase distributions are shown on top. Liquid track dryout is reached for $q = 2.5$ MW/m². The results are for $u_{l,o} = 0.5$ m/s.

difference across the interface between two phases. The instability criterion includes the velocity and density of each phase, as well as the surface tension [26] i.e.,

$$|u_g - u_l| < \left\{ \frac{2}{\rho_g^* \rho_l^*} \left[\frac{\sigma g (\rho_g^* - \rho_l^*)}{\rho_g^* + \rho_l^*} \right]^{1/2} \right\}^{1/2}, \quad (12)$$

where dimensionless densities are $\rho_k^* = \frac{\rho_k}{(\rho_g + \rho_l)}$. For saturated water-vapor flow, this threshold relative velocity is $|u_g - u_l| = 8.9$ m/s. The critical wavenumber is

$$\kappa_c = \frac{2g}{(u_g - u_l)^2} \frac{(\rho_g^* - \rho_l^*)}{\rho_g^* \rho_l^*} = \left[\frac{g(\rho_g^{*2} - \rho_l^{*2})}{\sigma} \right]^{1/2}, \quad (13)$$

where the critical wavelength is $\lambda_c = 2\pi/\kappa_c$. Using the geometric parameters of the FBCW, we related this wavelength at the channel

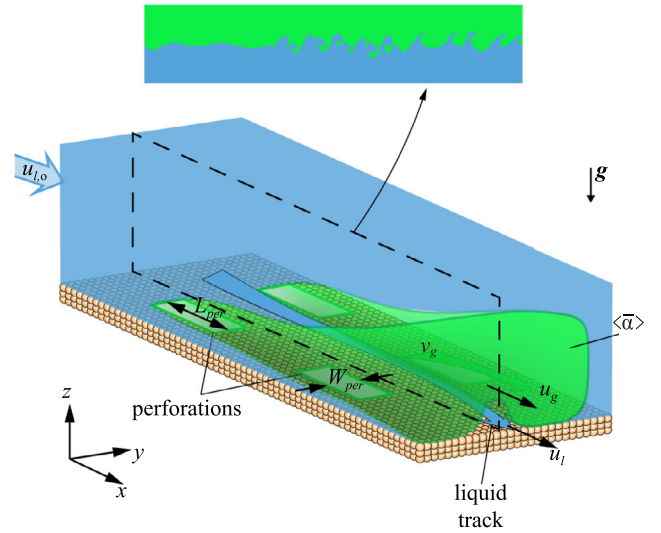
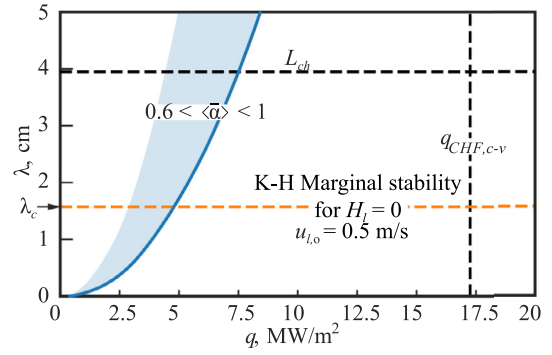


Fig. 10. Liquid-vapor interface above the leading-edge liquid track. Schematic representation of Kelvin-Helmholtz instabilities.

outlet as a function of heat flux as

$$\lambda_c = \frac{\pi (u_g - u_l)^2}{g} \frac{\rho_g^* \rho_l^*}{(\rho_g^* - \rho_l^*)} = \frac{\pi}{g} \left(\frac{q}{\rho_g \Delta h_{lg}} \frac{A_m}{\langle \alpha \rangle A_{ch}} - u_l \right)^2 \times \frac{\rho_g^* \rho_l^*}{(\rho_g^* - \rho_l^*)}, \quad (14)$$

where $\langle \alpha \rangle$ is the void fraction and the product $\langle \alpha \rangle A_{ch}$ the cross-section area occupied by the vapor. Figure 10 shows the results for water and the critical wavelength is 1.6 cm. The corresponding CHF from this simple analysis is about 2.5 MW/m², close to that found from the liquid track breakdown in Subsection 4.1 above. The void fraction can be obtained from the CFD and the results in Fig. 10 contemplate the range from 0.6 to 1.0. We now move to add levees to stabilize the liquid track and increase the CHF to the capillary-viscous limit marked in Fig. 10.

5. Stabilizing the liquid track with levees for enhanced CHF

The CHF predicted by CFD simulations for the FBCW is much smaller than the capillary-viscous limit of 17 MW/m², due to the liquid-vapor interaction, i.e., hydrodynamic limit. The continuity of the leading-edge liquid track disappears for a heat flux of about 2.0 to 2.5 MW/m².

In order to increase the CHF, 1 mm thick levees spanning the entire channel are added on the side of each perforation row to prevent the exiting vapor from spreading laterally and axially, disturbing the liquid stream. The front end of the vapor tracks are also closed to prevent vapor recoiling upstream which hinders the

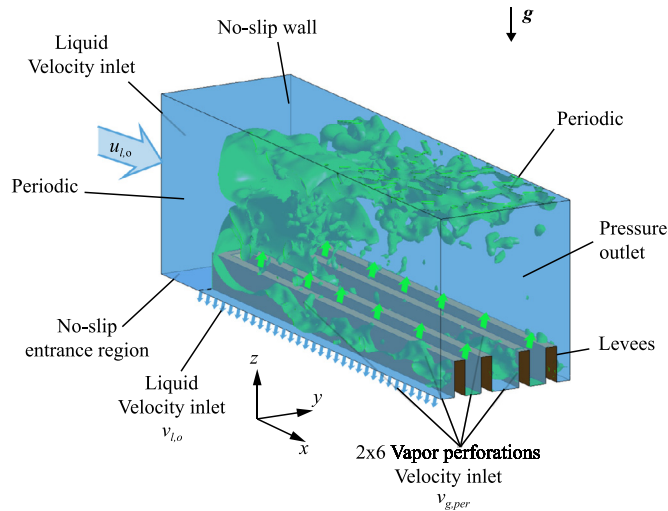


Fig. 11. The 2x6 perforations canopy wick with levees simulated (CFD) for the two-phase flow, showing the boundary conditions (irrigation of the wick and vapor escaping from perforations).

liquid entering the liquid track. This creates aquaducts and prevents dryout. This leveed 2x6 perforations FBCW domain used in the CFD simulations is shown in Fig. 11. An upstream, entrance length of 6 mm was added to allow for the liquid to enter the intralevee aquaducts or divert to the top of the channel. The levee walls are subjected to the velocity no-slip condition. As shows Fig. 1(a), the levees are porous structures sintered on top of the canopy. The levee height is $H_l = 3$ mm and the wall thickness is $l_l = 1$ mm, as mentioned earlier. The larger levee heights of 5 mm and 7.5 mm did not make a noticeable improvement (over the 3 mm height) up to 17 MW/m².

In contrast with the case of no levees in Section 4.3, the addition of levees even while reducing the available width for the leading-edge liquid track, isolates it from severe shear instability by the vapor exiting the perforations. The absence of lateral vapor shearing, diverting the vapor outward, and the geometric confinement of the liquid (anchoring to the levee walls) all assist in the stability of the liquid track. Fig. 12 shows the temporal variations of the liquid track height at the exit, for three different heat fluxes, for $u_{l,o} = 0.5$ m/s, up to 1.5 times the liquid particle transit time. The related phase distribution snapshots are shown on top. The leading-edge liquid track remains stable (not breaking and causing dryout) up to the end of the channel for very high heat flux (15 MW/m², below the capillary-viscous limit of 17 MW/m²), many folds over the CHF with no levees (about 2.0 to 2.5 MW/m²).

We now examine the levees mediated roles of the vapor diversion (which affects the Kelvin-Helmholtz instability) and the geometric liquid confinement (which anchors the liquid) on the CHF.

5.1. Vapor diversion by levees

Figures 13(a) to (c) show the perforation escaping vapor streamline without and with the levees, for heat fluxes below their corresponding CHF. The results are for $u_{l,o} = 0.5$ m/s. The blue background represents the liquid and the green bubble represents the vapor. Without levees, the instantaneous vapor streamlines spread both laterally (red color) as well outwardly (blue color). The vapor shearing thins and destabilizes the leading-edge liquid track, causing dryout (Fig. 9). The outward vapor flow does not effect the liquid track. As shown in Figs. 13(b) and (c), the addition of levees prevents the lateral vapor flow and divert that outward, protecting liquid track from shear instability. The vapor recoils and enters the aquaducts, but it does so at a much lower velocity, i.e., reduced in-

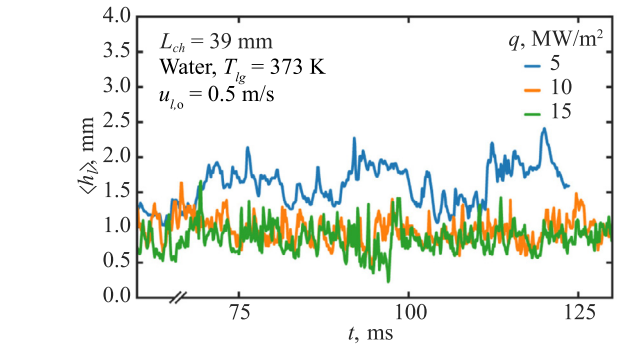
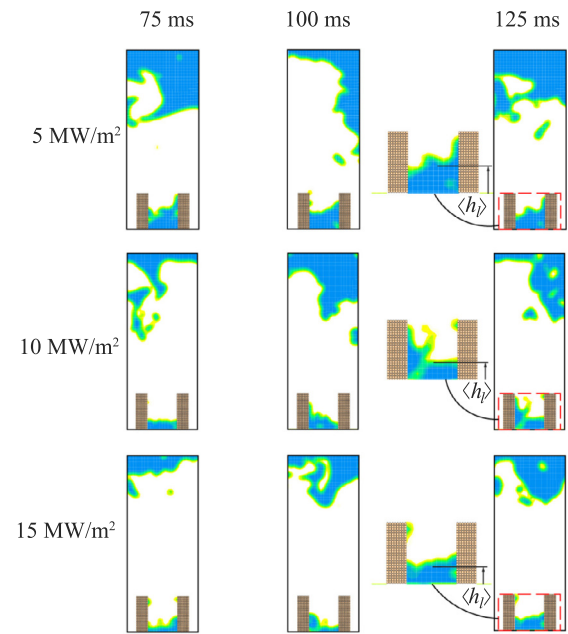


Fig. 12. Time variations of the average liquid track height at the channel outlet for three different heat flux. The corresponding snapshots of the outlet phase distributions are shown on top. The results are for $u_{l,o} = 0.5$ m/s.

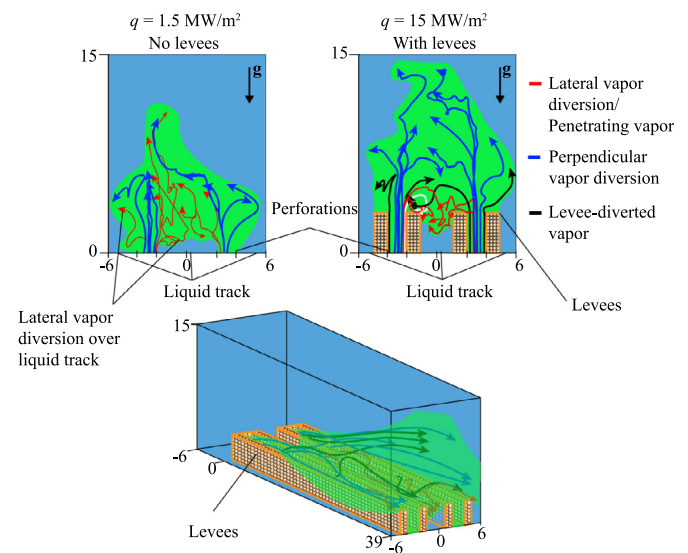


Fig. 13. Frontal view of the streamlines representation of the diversion of vapor caused by the addition of levees for: (a) $q = 5$ MW/m². (b) $q = 15$ MW/m² side view, and (c) perspective view with levees. The envelope of the vapor bubble is sketched by the dashed line. The results are for $u_{l,o} = 0.5$ m/s.

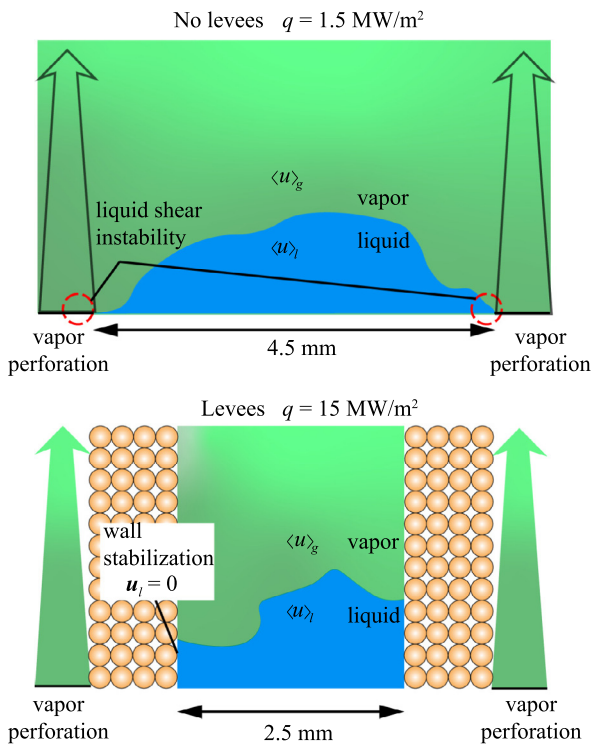


Fig. 14. Liquid track topology and the surrounding vapor at the channel exit. (a) The case on no levees leads to smaller CHF due to lateral spreading of the vapor exiting the perforations, and here the results are for $q = 1.5 \text{ MW/m}^2$. (b) With the levees, the vapor diversion and the levee wall-stabilize the liquid track.

terfacial shear. The black arrows represent vapor streamlines successfully diverted away from the liquid track, they flow over the intralevee channel without recoiling.

Figure 13(c) shows a perspective view of the entire channel for the leveed perforation and very high heat flux. The vapor expands laterally beyond the perforation rows, but its effect on the liquid track is greatly diminished. At $q = 15 \text{ MW/m}^2$ the height of the exit liquid track is nearly the same as the $q = 1.5 \text{ MW/m}^2$ without levees.

5.2. Wall geometric confinement of liquid track

Geometric confinement has a stabilizing effect on the liquid track [27]. This is illustrated in Figs. 14(a) and (b), with and without levees. Addition of levees to the side of the perforations allows for the liquid confinement between them and shields the liquid from the lateral shearing. The walls anchor the liquid (no-slip condition), requiring additional shear from the vapor flow to disturb the liquid track. Both the liquid and vapor phases experience the same pressure gradient (neglecting inertial effects) within the aquaduct, so there is a measure of local mechanical equilibrium between the phases.

So the vapor diversion by the levees protects the liquid track from the lateral vapor shear and the only interfacial interaction is due to the relative axial velocity at the interface. In addition the geometric liquid confinement further stabilizes the liquid track. We now examine the contributions of these two stabilizing effect which extend the dryout, using the CFD results. Figures 15(a) and (b) show the CFD predicted variations of the vapor-liquid interfacial velocity slip (volume averaged over the phases) and the averaged exit liquid track height, with respect to the imposed heat flux.

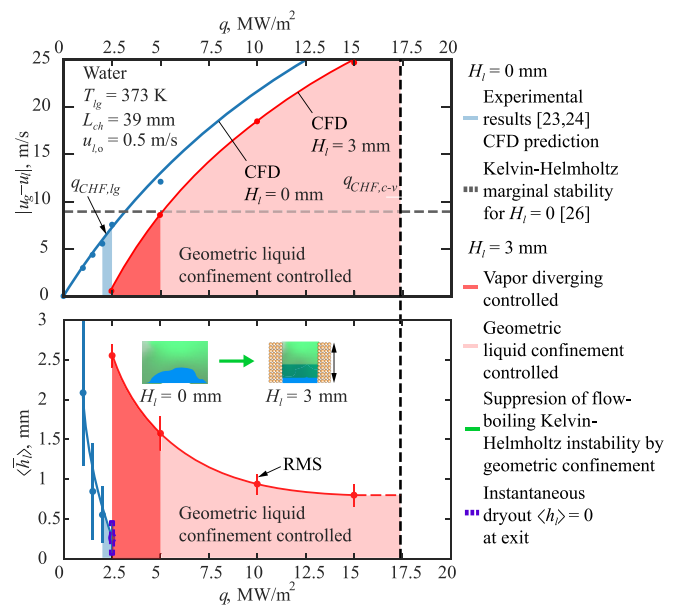


Fig. 15. Variations of CFD predicted channel exit (a) interfacial relative phase velocity, and (b) time-averaged liquid track height, with respect to the heat flux. The results are for cases without and with levees and for $u_{t,o} = 0.5 \text{ m/s}$.

In Fig. 15, the Kelvin-Helmholtz limit and the capillary-viscous limits are also shown. The results are for no-levees geometry as well as with levees of height 3 mm. The CFD predicted and experimental result for CHF without levees are also shown. The results show the interfacial relative velocity decreases with the presence of the levees. This is due to the vapor diversion. We also note that even under very high heat flux where the relative velocity is larger than the critical value predicted by Eq. (12), the liquid track remains stable, Fig. 15(b), and CHF is delayed. This indicates that liquid geometric confinement prevents the development of Kelvin-Helmholtz instability.

The CFD simulations show that at high heat flux, the escaping vapor still manages to disturb the liquid track by entering from the open top surface of the duct, but even with high relative velocities, the Kelvin-Helmholtz instability cannot suppress the leading-edge liquid track. So in Fig. 15(a), we mark the enhancement of the CHF by the levees into two regimes. The first is by the vapor diversion and the second by the liquid geometric confinement, where the latter has a much larger and impacting extent.

5.3. Effect of liquid inlet velocity

The added stability provided by the levees allows for lower inlet liquid velocities without affecting the leading-edge liquid track height inside the levees. Fig. 16 shows the axial variations of instantaneous liquid track height for three liquid inlet velocities, 0.5, 0.2, and 0.05 m/s at $y = 1 \text{ mm}$. Local dryout is observed for the lowest velocity, 0.05 m/s, and illustrated by the snapshots of phase distribution.

The inlet velocity affects also the exit (at L_{ch}) temporal-spatial averaged void fraction and quality, and the inlet velocity enhancement defined as a measure of the convergence of inlet liquid into the intralevee aquaducts. These are listed in Table 2. The quality is calculated using the void fraction outlined in [28]. The thermal conductance (G/A) discussed in Subsection 3.2 is expected to be the same for all three cases, while the exit quality increases with decreasing velocity. The exit void fraction is larger than 0.9 for all three cases. So, the FBCW allows for using smaller liquid

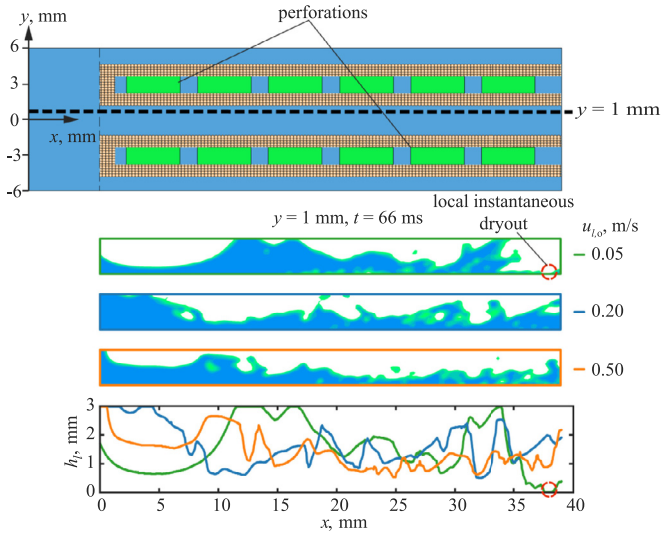


Fig. 16. Axial variations (at $y = 1$ mm, marked with broken line) of the liquid track height for different inlet velocities for $t = 66$ ms. Local dryout occurs for the lowest velocity and also shown by snapshots of the phase distribution of the intralevee flow.

Table 2

Effect of inlet liquid velocity on the temporal-spatial averaged void fraction and vapor quality at the exit, and the liquid flow enhancement at the intralevee entrance and Froude number. The results are for $q = 15$ MW/m².

$u_{l,o}$, m/s	$\langle \bar{\alpha} \rangle$	$\langle \bar{x} \rangle$	$\langle \bar{u}_1 \rangle_o / u_{l,o}$	$Fr_{D,per}$
0.05	0.958	0.148	5.84	0.34
0.2	0.9532	0.095	2.03	1.34
0.5	0.862	0.048	1.51	3.36

inlet velocity while keeping both the dryout limit (CHF) and the thermal conductance much larger than those for the plain surface. This would make for a more efficient use of the liquid stream for evaporation. The effect of gravity, represented by the Froude number, is also shown. The results are for $q = 15$ MW/m² and $H_l = 3$ mm, and $L_{ch} = 3.9$ cm, and the liquid track persists up to the exit (no dryout) even with liquid inlet velocity (0.1 m/s). However, the Froude number becomes smaller than unity for this inlet velocity.

6. Summary of results

6.1. Water

The predicted CHF (left vertical axis) and G/A (right vertical axis) for the flow boiling (in a channel with horizontal, upward heated surface) with and without the FBCW coating are shown in Fig. 17(a), along with various limits. The results are for saturated water at 1 atm, and with $u_{l,o} = 0.2$ m/s (as a typical low velocity, and for 0.1 m/s the results are similar). The results for the FBCW are for a 2x6 perforation corresponding to a heated channel length of 39 mm. The geometric parameters are listed in Table 3.

The limits on the CHF are: starting from the lowest, the Zuber pool boiling ($q_{CHF,z}$), the experimental results for the plain surface ($q_{CHF,ps}$), the capillary-viscous ($q_{CHF,c-v}$), the superheat ($q_{CHF,sh}$), the vapor compressibility ($q_{CHF,ma}$), vapor choking at perforation ($q_{CHF,ch}$), and the kinetic theory (q_{max}). The red bar on the left accounts for the effect of a non-ideal monolayer, the bottom end pre-

sents loose packing, lower capillary pressure, and the top end hexagonal packing, lower capillary pressure. The limits and bench marks for the G/A are, starting with the lowest, the experimental results for the plain surface (G/A)_{ps}, the FBCW performance (G/A)_{FBCW}, the conductance of 1 mm of pure copper (G/A)_{Cu}, and the conductance of 1 mm synthetic diamond (G/A)_{diamond}.

The lower portion of Fig. 17(a) shows the performance of the plain surface (Section 4). The experimental results are also for $u_{l,o} = 0.2$ m/s, with $q_{CHF,ps}$ of about 1.5 MW/m² as typical [23,24], and (G/A)_{ps} of about 75 kW/m²-K is also typical and strongly local vapor-quality dependent [29] (deteriorates very quickly for vapor quality larger than 0.1 [25]). The use of the modified interfacial lift-off model from [9] gives $q_{CHF,ps} = 1.5$ MW/m², in agreement with the reported experimental results. The original interfacial lift-off model [7] is unstable for $u_{l,o} < 1$ m/s.

Addition of the FBCW and creation of the vapor space underneath the canopy and evaporation on the thin monolayer increases the thermal conductance and the (G/A)_{FBCW} is twice as large as the plain surface value, as shown in Fig. 17(a). This was observed with or without the levees. This (G/A)_{FBCW} is still below the (G/A)_{Cu}, so in typical heat transfer devices the evaporator resistance is still important compared to conduction resistance through the metallic membranes.

The FBCW with levees increases the CHF substantially over the plain surface, provided the monolayer capillary pressure can reach the ideal packing value which for the FBCW listed in Table 3 gives $q_{CHF,c-v} = 17$ MW/m². This enhancement is represented by the dimensionless figure of merit Z_{FBCW} , defined as [12]

$$Z_{FBCW} = \frac{q_{CHF,FBCW}}{q_{CHF,ps}} \frac{(G/A)_{FBCW}}{(G/A)_{ps}}, \quad (15)$$

where the plain surface CHF $q_{CHF,ps}$ and thermal conductance (G/A)_{ps} are shown in Fig. 17(a). The Z_{FBCW} of 20 demonstrates the advantage of the FBCW over plain surface flow boiling.

6.2. FC-72

Direct simulations and local volume averaged properties have also been calculated for the FC-72 as working fluid (saturated at 1 atm). The maximum capillary pressure is smaller than water (4.18 kPa compared with 16.2 kPa), mostly due to its lower surface tension.

Figure 17 (b), shows the performance of the plain surface. The experimental results are also for $u_{l,o} = 0.05$ m/s, with $q_{CHF,ps}$ of about 0.25 MW/m² as typical [8], and (G/A)_{ps} of about 15 kW/m²-K is also typical and strongly local vapor quality dependent [30]. Additionally, two other values are shown for the plain surface CHF, using the interfacial lift-off model described in Part II Section 1. The prediction of model [7] with $u_{l,o} = 1$ m/s (solution not stable below this), gives $q_{CHF,ps} = 0.3$ MW/m² marked as the upper limit of the shaded region in the left axis. Its revised model [9] for $u_{l,o} = 0.25$ m/s, gives $q_{CHF,ps} = 0.18$ MW/m², the lower limit. The experimental result of [8] is also shown.

The FC-72 FBCW results are for four evaporator wicks and optimal geometry, namely: (i) monolayer (ideal packing $p_{c,max}$) and (ii) monolayer [bulk $p_{c,max}$ [31]] with $d_m = 50$ μ m, and (iii) bilayer and (iv) trilayer with $d_m = 100$ μ m and bulk $p_{c,max}$ to allow for packing irregularity. Using the local, meniscus-thickness dependent monolayer properties for (i) gives $q_{CHF,c-v} = 0.47$ MW/m², while (ii) gives $q_{CHF,c-v} = 0.25$ MW/m². The bilayer and trilayer evaporators perform similar to (i). The extra layers help reduce the evaporator pressure drop component (increase in the cross-sectional area), however, the thermal conductance deteriorates. Evaporator (i) gives (G/A)_{FBCW} = 0.057 MW/m²-K, four fold increase over the

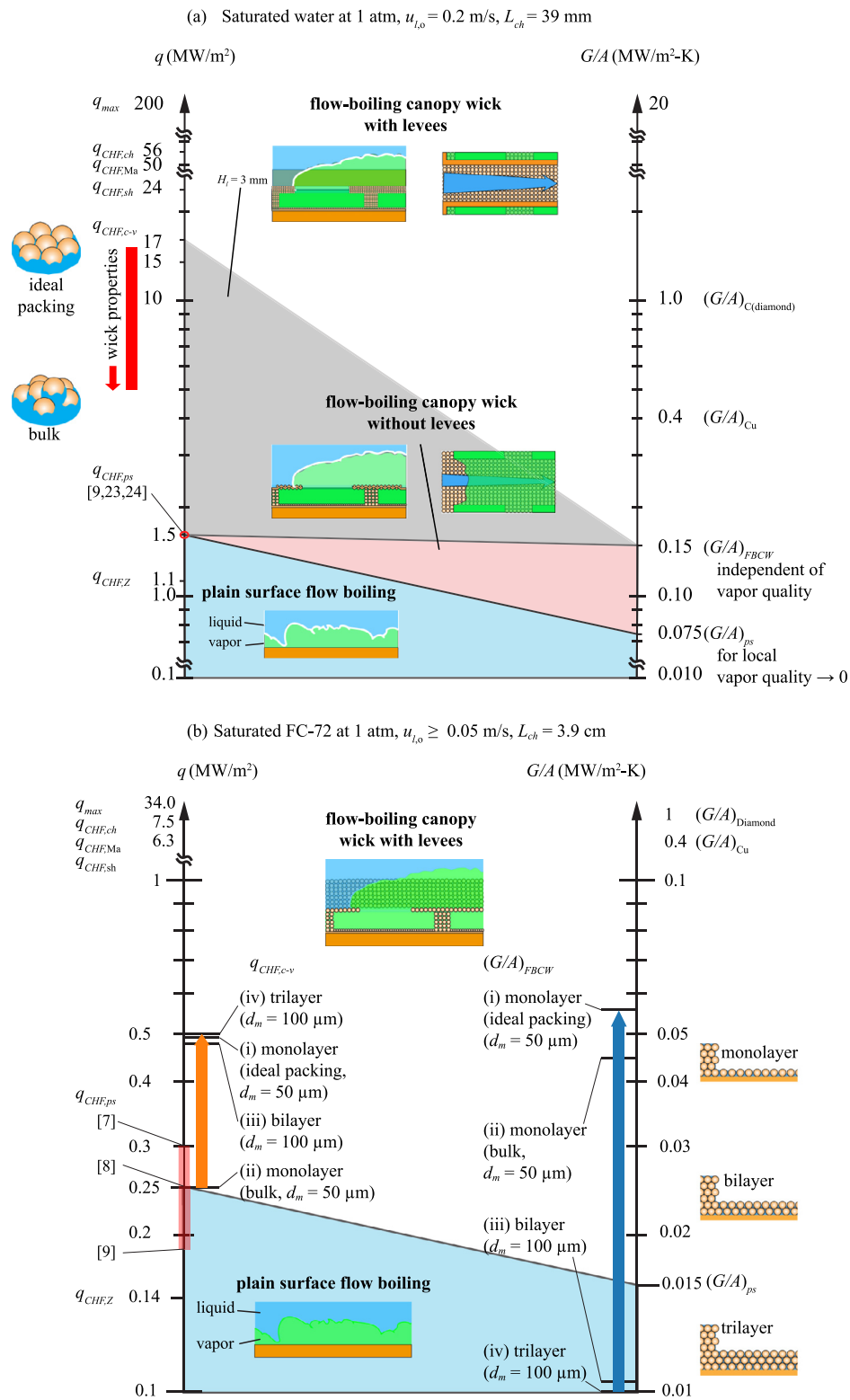


Fig. 17. Various limits on the flow-boiling CHF and thermal conductance (G/A) for plain surface and for surface coated with FBCW with and without the levees. The ideal particle packing of the monolayer wick gives the largest capillary pressure, and therefore, the capillary-viscous limit controls the CHF. With a non-ideal (loose) packing this CHF decreases. This is depicted on the left side. Various limits and benchmarks for both CHF and G/A are also marked. (a) Saturated water at 1 atm. (b) Saturated FC-72 at 1 atm.

Table 3

Summary of FBCW main parameters, by row: heat flux, channel flow and fluid properties; unit cell, perforation and post geometry; dimensionless numbers; pressure drop components and wicking length; thermal conductance, superheating and performance measure. The CHF enhancement (hydrodynamic instability delay) is caused by diverting the vapor exiting the canopy wick perforation and stabilizing the leading-edge liquid track between perforations with the levee walls. A video of the flows is available in the [Supplementary Materials](#).

q (MW/m ²)	$u_{l,o}$ (m/s)	$v_{g,o}$ (m/s)	$v_{l,o}$ (cm/s)	ρ_l/ρ_g	μ_l/μ_g
15	0.2	61.2	0.85	1622	23
H_{ch} (mm)	L_{ch} (mm)	W_{ch} (mm)	L_{per} (mm)	H_l (mm)	l_l (mm)
15	39	12	4.5	3	1
W_{per} (mm)	Δ_p (mm)	$N_{p,x}$	ϵ_m, d_m (μm)	ϵ_p, K_p (μm^2)	ϵ_{ca}, K_{ca} (μm^2)
1.5	0.5	4	0.40, 50	0.35, 1.41	0.35, 1.41
Re_l	Re_g	$We_{D,c}$	$Fr_{D,per}$	$Ma_{g,o}$	
1×10^3	6.2×10^3	3.9	1.34	0.15	
Δp_{ca} (kPa)	Δp_p (kPa)	Δp_m (kPa)	$\Delta p_{per,g}$ (kPa)	$\Sigma \Delta p_i$ (kPa)	$p_{c,max}$ (kPa)
0.4	2	7	3.9	13.4	16.2
G/A (MW/m ² -K)	$T_s - T_{lg}$ (K)	$\Delta T_{sh,max}$ (K)	Z_{FBCW}		
0.15	100	160.4	20		

Table 4

Summary of the FBCW parameters and results for FC-72, using four evaporators, by row: heat flux, channel flow and fluid properties; unit cell, perforation and post geometry; dimensionless numbers; pressure drop components and wicking length; thermal conductance, superheating and performance measure. The CHF enhancement (hydrodynamic instability delay) is caused by diverting the vapor exiting the canopy wick perforation and stabilizing the leading-edge liquid track between perforations with the levees. A video of the flows is available in the [Supplementary Materials](#).

Evaporator	q (MW/m ²)	G/A (MW/m ² -K)	$T_s - T_{lg}$ (K)	$\Delta T_{sh,max}$ (K)	Z_{FBCW}
Monolayer	0.47	0.057	8.2	50	7.14
Monolayer (bulk)	0.25	0.044	5.6		2.93
Bilayer	0.46	0.012	40.2		1.43
Trilayer	0.49	0.008	64		1.01
$u_{l,o}$ (m/s)	$v_{g,o}$ (m/s)	$v_{l,o}$ (cm/s)	ρ_l/ρ_g	μ_l/μ_g	
0.05	2.53	2.67	122	34.9	
	1.32	1.39			
	2.03	2.14			
	2.15	2.27			
H_{ch} (mm)	L_{ch} (mm)	W_{ch} (mm)	L_{per} (mm)	H_l (mm)	l_l (mm)
15	39	10	4.5	3	1
		10.5			
W_{per} (mm)	Δ_p (mm), $N_{p,x}$	ϵ_m, d_m (μm)	$\langle \delta_m \rangle$ (μm)	ϵ_p, K_p (μm^2)	ϵ_{ca}, K_{ca} (μm^2)
0.5	0.5, 4	0.40, 50	31.4	0.35, 1.41	0.35, 1.41
		0.40, 50	37.5	1	
0.75		0.40, 100	200	0.35, 5.63	0.35, 5.63
		0.40, 100	300		
Re_l	Re_g	$We_{D,c}$	$Fr_{D,per}$	$Ma_{g,o}$	
0.3×10^3	2.5×10^3	2.3	0.54	0.006	
	1.6×10^3			0.003	
	2.9×10^3	2.4	0.44	0.005	
	3.1×10^3			0.005	
Δp_{ca} (Pa)	Δp_p (Pa)	Δp_m (Pa)	$\Delta p_{per,g}$ (Pa)	$\Sigma \Delta p_i$ (Pa)	$p_{c,max}$ (Pa)
94	777	2488	822	4185	4185
49	402	1138	221	1813	1813
24	214	236	432	907	907
25	227	167	486	907	907

plain surface value. For (ii), using the effective thermal conductivity discussed in Part II Section 3, the thermal conductance increases by three folds. On the other hand, cases (iii) and (iv) the thermal conductance is below the plain surface. So for the CHF and the thermal conductance enhancements, different evaporators should be used, and when combining the optimal performance the dimensionless figure of merit Z_{FBCW} should be used. This enhancement for the monolayer with the ideal packing is over 6 folds compared to plain surface.

The above results are summarized in [Table 4](#). Thermal conductance results are valid with or without the levees. This $(G/A)_{FBCW}$

is still below the $(G/A)_{Cu}$, so in typical heat transfer devices the evaporator resistance is still important compared to conduction resistance through the metallic membranes. The addition of levees, similar to the case for water discussed in [Subsection 6.1](#), allows for a lower liquid inlet velocity without compromising the CHF.

Compared to water, FC-72 has smaller surface tension and a larger liquid viscosity, which results in smaller maximum capillary pressure and larger pressure drop. The mass flow rates are high even at relatively low heat flux, due to the lower heat of evaporation, reducing the $q_{CHF,c-v}$. The use of FBCW allows for using smaller $u_{l,o}$.

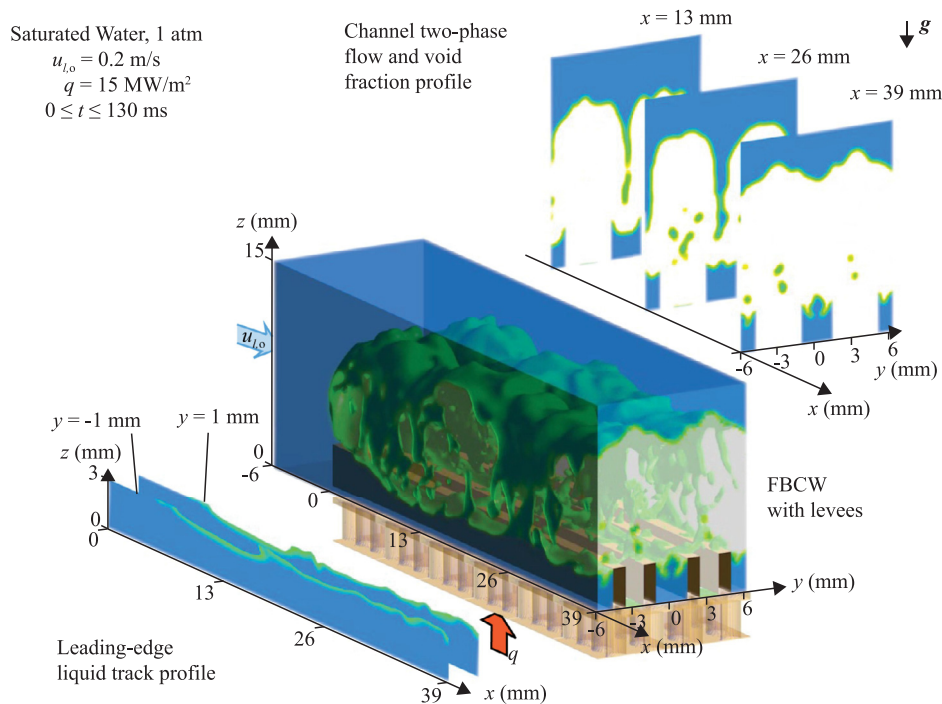


Fig. 18. Phase distributions and flows above and below the canopy wick for the CFD simulated 2x6 perforations FBCW, with snapshots of the phase distributions along selected axial and lateral locations. A video of the flows is available in the [Supplementary Materials](#).

7. Conclusions

Enhancement of flow-boiling CHF and thermal conductance in horizontal channel heated from the lower surface with the FBCW (flow-boiling canopy wick) is investigated using CFD simulations and stability analysis. The perforated canopy allows for formation of a leading-edge liquid tracks between the perforation which are subject to shear instability as vapor accumulates momentum downstream. So, by adding levees to this 3-D porous structure hydrodynamic instability is suppressed allowing for continuous liquid supply to the heated surface for heat flux up the capillary-viscous limit.

The specific predicted results for 3.9 cm long heated section covered by the unit-cell based FBCW are a heat flux in excess of 15 MW/m² for the water-copper wick and high thermal conductance of 150 kW/m²-K. Without the levees the CHF is about 2.5 MW/m², close to the plain surface value. These represent a 20 fold enhancement over the plain surface measured by the figure of merit defined in Section 6.

The capillary-viscous CHF is controlled by the maximum capillary pressure which occurs in the monolayer, and the packing of the sintered particles is critical, with the close packing of a single layer giving the highest $p_{c,max}$ and the randomly packed multilayer given by the lower bulk $p_{c,max}$. Left of Fig. 17, this effect on the $q_{CHF,c-v}$ is shown, with the lower limit based on the bulk, random packing $p_{c,max} = 4\sigma / (C_r d_m)$ of 12.6 kPa, where $C_r = 0.375$ [31].

Table 3 summarized the wick parameters, flow condition and properties, and predicted performance of the leveed FBCW for water. The results are for $u_{l,o} = 0.2$ m/s, i.e., a rather low liquid velocity, thus making this a very efficient use of the liquid stream for removing high heat flux. Similarly, Table 4 shows these results for FC-72.

Figure 18 shows a snapshot of the related video of the phase distributions and flows above and below the canopy wick for water for the CFD simulated 2x6 perforations FBCW vapor exiting

the canopy wick perforation and stabilizing the leading-edge liquid track between perforations with the levee walls. Snapshots of the phase distributions along selected axial and lateral locations are also shown. These are explained using CFD predictions and a Kelvin-Helmholtz instability analysis. Additionally, a video of the phase distributions and flows above and below the canopy for FC-72 for the CFD simulated 2x6 perforations FBCW with levees is linked here <https://doi.org/10.1016/j.ijheatmasstransfer.2020.120080>.

The investigation of the hydrodynamic control of the boiling crises with FBCW capillary surface structure for two fluids allows for thermal control of high heat flux systems and also allows for insights into the boiling phenomena.

Declaration of Competing Interests

The authors declare that they have no known competing financial interests or personal relationships that could have appeared to influence the work reported in this paper.

CRediT authorship contribution statement

Júlio Ferreira: Conceptualization, Methodology, Formal analysis, Visualization, Writing - original draft. **Massoud Kaviany:** Validation, Resources, Supervision, Project administration.

Acknowledgements

This work is supported by NSF USA (Thermal Transport and Processes, CBET16235720). JF is thankful and acknowledges his scholarship supported by CAPES - Brazilian Federal Agency for Support and Evaluation of Graduate Education within the Ministry of Education. We are thankful to Minki Kim for his technical guidance.

Supplementary material

Supplementary material associated with this article can be found, in the online version, at doi:[10.1016/j.ijheatmasstransfer.2020.120080](https://doi.org/10.1016/j.ijheatmasstransfer.2020.120080).

References

- [1] M. Kim, M. Kaviany, Flow-boiling canopy wick for extreme heat transfer, *International Journal of Heat and Mass Transfer* 117 (2018) 1158–1168, doi:[10.1016/j.ijheatmasstransfer.2017.10.079](https://doi.org/10.1016/j.ijheatmasstransfer.2017.10.079). <http://www.sciencedirect.com/science/article/pii/S0017931017334579>.
- [2] S.M. Ghiaasiaan, *Critical Heat Flux and Post-CHF Heat Transfer in Flow Boiling*, Cambridge University Press, 2007. Ch. 13, pp. 371–404. DOI:10.1017/CBO9780511619410.016.
- [3] C. Konishi, I. Mudawar, Review of flow boiling and critical heat flux in microgravity, *International Journal of Heat and Mass Transfer* 80 (2015) 469–493, doi:[10.1016/j.ijheatmasstransfer.2014.09.017](https://doi.org/10.1016/j.ijheatmasstransfer.2014.09.017). <http://www.sciencedirect.com/science/article/pii/S0017931014008096>.
- [4] M. Bruder, G. Bloch, T. Sattelmayer, Critical heat flux in flow boiling review of the current understanding and experimental approaches, *Heat Transfer Eng.* 38 (3) (2017) 347–360, doi:[10.1080/01457632.2016.1189274](https://doi.org/10.1080/01457632.2016.1189274).
- [5] L. Tong, Boundary-layer analysis of the flow boiling crisis, *International Journal of Heat and Mass Transfer* 11 (7) (1968) 1208–1211, doi:[10.1016/0017-9310\(68\)90037-9](https://doi.org/10.1016/0017-9310(68)90037-9). <http://www.sciencedirect.com/science/article/pii/0017931068900379>.
- [6] S.S. Kutateladze, A.I. Leontev, Some applications of the asymptotic theory of the turbulent boundary layer, in: *International Heat Transfer Conference*, Vol. 3, 1966. Pp. 1–6.
- [7] J. Sturgis, I. Mudawar, Critical heat flux in a long, rectangular channel subjected to one-sided heating-II. Analysis of critical heat flux data, *International Journal of Heat and Mass Transfer* 42 (10) (1999) 1849–1862, doi:[10.1016/S0017-9310\(98\)00275-0](https://doi.org/10.1016/S0017-9310(98)00275-0). <http://www.sciencedirect.com/science/article/pii/S0017931098002750>.
- [8] H. Zhang, I. Mudawar, M.M. Hasan, Experimental and theoretical study of orientation effects on flow boiling chf, *International Journal of Heat and Mass Transfer* 45 (22) (2002) 4463–4477, doi:[10.1016/S0017-9310\(02\)00152-7](https://doi.org/10.1016/S0017-9310(02)00152-7). <http://www.sciencedirect.com/science/article/pii/S0017931002001527>.
- [9] C.-N. Huang, C.R. Kharangate, A new mechanistic model for predicting flow boiling critical heat flux based on hydrodynamic instabilities, *International Journal of Heat and Mass Transfer* 138 (2019) 1295–1309, doi:[10.1016/j.ijheatmasstransfer.2019.04.103](https://doi.org/10.1016/j.ijheatmasstransfer.2019.04.103). <http://www.sciencedirect.com/science/article/pii/S001793101930167X>.
- [10] V.P. Carey, *Convective boiling in tubes and channels*, Taylor & Francis (1992). Ch. 12, pp. 483–562.
- [11] Y. Haramura, Y. Katto, A new hydrodynamic model of critical heat flux, applicable widely to both pool and forced convection boiling on submerged bodies in saturated liquids, *International Journal of Heat and Mass Transfer* 26 (3) (1983) 389–399, doi:[10.1016/0017-9310\(83\)90043-1](https://doi.org/10.1016/0017-9310(83)90043-1). <http://www.sciencedirect.com/science/article/pii/0017931083900431>.
- [12] M. Kim, M. Kaviany, Multi-artery heat-pipe spreader: monolayer-wick receding meniscus transitions and optimal performance, *International Journal of Heat and Mass Transfer* 112 (2017) 343–353, doi:[10.1016/j.ijheatmasstransfer.2017.04.131](https://doi.org/10.1016/j.ijheatmasstransfer.2017.04.131). <http://www.sciencedirect.com/science/article/pii/S0017931017306889>.
- [13] J. Ferreira, M. Kaviany, Geometric-confinement suppression of flow-boiling instability using perforated wick: part II CHF limits and wick properties, *Int. J. Heat Mass Transf.* 159 (2020) 120079.
- [14] M. Kaviany, *Principles of Heat Transfer in Porous Media*, 2nd Edition, Springer, 1995.
- [15] S. Modak, M. Kaviany, S. Hoenig, R. Bonner, Numerical analysis of meniscus dynamics in monolayer-wick dropwise condensation, *Numerical Heat Transfer, Part A: Applications* 76 (5) (2019) 301–322, doi:[10.1080/10407782.2019.1627829](https://doi.org/10.1080/10407782.2019.1627829).
- [16] A.J. Ward-Smith, R.P. Benedict, W.M. Hagist, Internal fluid flow: The fluid dynamics of flow on pipes and ducts and fundamentals of pipe flow, *Journal of Fluids Engineering* 104 (1) (1982), doi:[10.1115/1.3240841](https://doi.org/10.1115/1.3240841). 129–129.
- [17] K.A. Brakke, The surface evolver, *Exp. Math.* 1 (2) (1992) 141–165, doi:[10.1080/10586458.1992.10504253](https://doi.org/10.1080/10586458.1992.10504253).
- [18] G. Hadley, Thermal conductivity of packed metal powders, *International Journal of Heat and Mass Transfer* 29 (6) (1986) 909–920, doi:[10.1016/0017-9310\(86\)90186-9](https://doi.org/10.1016/0017-9310(86)90186-9). <http://www.sciencedirect.com/science/article/pii/0017931086901869>.
- [19] Siemens, STAR-CCM+ user manual, 2020.
- [20] ANSYS, Fluent reference manual, 2009.
- [21] Y. Murai, Frictional drag reduction by bubble injection, *Exp. Fluids* 55 (1773) (2014) 1–28, doi:[10.1007/s00348-014-1773-x](https://doi.org/10.1007/s00348-014-1773-x).
- [22] D. Kim, P. Moin, Direct numerical simulation of air layer drag reduction over a backward-facing step, *Center for Turbulence Research - Annual research brief (2010)* 351–363.
- [23] T. Lee, D.H. Kam, J.H. Lee, Y.H. Jeong, Effects of two-phase flow conditions on flow boiling chf enhancement of magnetite-water nanofluids, *Int. J. Heat Mass Transf.* 74 (2014) 278–284, doi:[10.1016/j.ijheatmasstransfer.2014.03.028](https://doi.org/10.1016/j.ijheatmasstransfer.2014.03.028).
- [24] H. Sakashita, A. Ono, J. Nyui, Critical heat flux and near-wall boiling behaviors in saturated and subcooled pool boiling on vertical and inclined surfaces, *J. Nucl. Sci. Technol.* 46 (11) (2009) 1038–1048, doi:[10.1080/18811248.2009.9711614](https://doi.org/10.1080/18811248.2009.9711614).
- [25] X. Fang, Z. Zhou, H. Wang, Heat transfer correlation for saturated flow boiling of water, *Appl. Therm. Eng.* 76 (2015) 147–156, doi:[10.1016/j.applthermaleng.2014.11.024](https://doi.org/10.1016/j.applthermaleng.2014.11.024).
- [26] S. Chandrasekhar, *The stability of superposed fluids: the Kelvin-Helmholtz instability*, *International series of monographs on physics*, Clarendon Press, 1961. Ch. 11, pp. 481–514.
- [27] K.J. Humphry, A. Ajdari, A. Fernández-Nieves, H.A. Stone, D.A. Weitz, Suppression of instabilities in multiphase flow by geometric confinement, *Physical Review E* 79 (5) (2009) 056310, doi:[10.1103/PhysRevE.79.056310](https://doi.org/10.1103/PhysRevE.79.056310).
- [28] S.M. Zivi, Estimation of steady-state steam void-fraction by means of the principle of minimum entropy production, *J. Heat Transfer* 86 (2) (1964) 247–251, doi:[10.1115/1.3687113](https://doi.org/10.1115/1.3687113).
- [29] S.G. Kandlikar, A general correlation for saturated two-phase flow boiling heat transfer inside horizontal and vertical tubes, *J. Heat Transfer* 112 (1) (1990) 219–228, doi:[10.1115/1.2910348](https://doi.org/10.1115/1.2910348).
- [30] S.-M. Kim, I. Mudawar, Universal approach to predicting saturated flow boiling heat transfer in mini/micro-channels part II. two-phase heat transfer coefficient, *International Journal of Heat and Mass Transfer* 64 (2013) 1239–1256, doi:[10.1016/j.ijheatmasstransfer.2013.04.014](https://doi.org/10.1016/j.ijheatmasstransfer.2013.04.014). <http://www.sciencedirect.com/science/article/pii/S0017931013003190>.
- [31] S.G. Lister, M. Kaviany, Pool-boiling CHF enhancement by modulated porous-layer coating: theory and experiment, *International Journal of Heat and Mass Transfer* 44 (22) (2001) 4287–4311, doi:[10.1016/S0017-9310\(01\)00084-9](https://doi.org/10.1016/S0017-9310(01)00084-9). <http://www.sciencedirect.com/science/article/pii/S0017931001000849>.